D-Band Thin-Film Resistive Line Bolometer as Transfer Standard

Kamble, Harshwardhan; Salek, Milan; Wang, Xueshen; Celep, Murat; Stokes, Daniel; Skinner, James; Wang, Yi

[Link to publication on Research at Birmingham portal](#)

D-band Thin-Film Resistive Line Bolometer as Transfer Standard

Harshwardhan Kamble, Milan Salek, Xueshen Wang, Murat Celep, *Senior Member, IEEE*, Daniel Stokes, James Skinner, *Member, IEEE*, Yi Wang, *Senior Member, IEEE*

Abstract— A bolometric thin-film based transfer standard with a novel structure for absolute power detection in D-band (110 - 170 GHz) is reported. It uses a resonance-type matching technique with thin-film resistive lines. The same line functions as the sensing element. The change in the resistivity of the line under the incident wave is calibrated to measure the absolute RF power in the D-band. This paper presents the analysis using equivalent circuit models, the full-wave electromagnetic design, the fabrication and the comprehensive characterization of the device. The comparison between a single and a folded-line matching structure is performed, showing the wideband capability of the latter. The transfer standard consists of two sensors in one waveguide housing for RF power measurement, as well as for monitoring and calibrating out the ambient temperature variation. It has shown a very good short-term time response with only ~0.19 % deviation in a given time interval, which is very close to a commercial PM5 sensor with ~0.27 % deviation. The long-term time response is also impressive, with a deviation of less than 0.6 %, similar to a commercial PM5 sensor. The fast response time, good thermal isolation and ambient compensation ability make it suitable for transfer/working standards, which can be used in ambient temperature environments.

Index Terms— Barretter mount, bolometer, metrology millimetre wave, power sensor, thin-film, transfer standard.

I. INTRODUCTION

IN the electromagnetic spectrum, microwave (3 – 30 GHz) and millimetre-wave (30 - 300 GHz) bands have a major contribution in communication, defence, astronomy, and medical applications. However, the sub-terahertz (sub-THz) band above 100 GHz is not substantially commercialised [1]. Today this band is mostly used for scientific research. One of the reasons why this band has been immature for many years is the manufacturing challenges at very short wavelengths (λ < 3 mm). Considerable research is going on to utilise this band by employing advanced fabrication techniques such as high-precision CNC machining, micromachining and 3D printing [2]. Another reason is that very few commercial sources and detectors are readily available, as solid-state devices often suffer from excessive losses and limited efficiency [1]. In the past few years, the commercial exploitation of the sub-THz band, especially around the D-band (110 - 170 GHz), is gaining momentum because of the emerging applications in back-haul communications and high-resolution radars. With these also comes the increasing demand for power measurement above 110 GHz for metrology and qualification.

One of the most demonstrated power measurement techniques is the calorimetric technique which is frequency independent [3], [4], and uses matched-load usually made of absorptive materials on tapered sections. Sensor elements employed include thermoelectric (single load [5], dual load [6], quasi twin [7]) or bolometric (thermistor [8], thin film [4], [9]) types. Such loads are also used as power-absorbing terminals in a twin-load configuration [10], [11]. However, the calorimeter is a primary power measurement standard and requires a very long heat settling time due to its bulky structure and high thermal mass [3], [4], [7]. A traceable/working standard (not only as a calorimetric load) is required for commercial users with a simple design and fast response time. The power detector in this paper is designed for such purposes.

Above 100 GHz, building a thermistor bead or platinum wire bolometer in a waveguide is difficult due to the space constraint, and their losses would significantly reduce the efficiency. Therefore, barretter mount based designs using metallic thin-film lines are adopted in this work. Similar techniques have been reported in [12]–[16] but at much lower frequencies. So far, the highest operation frequency of room temperature thin-film bolometer barretter mount is at 94 GHz reported in 1985 [15]. Some existing power standards are compared in Table I. We intend to compare all the metrology sensors above 75 GHz. Most of them are based on matched load. We also include three lower frequency sensors [12] [18] [24] as examples of the resonant-type sensor. Unfortunately, not all the key parameters (such as settling time) are provided in the literature. Some of the comparisons may be further qualified depending on the power level and scale used in the measurement. Some of the response time data were taken as an estimate from the figure provided in the literature.

In this paper, a novel thin-film resistive-line based power detector is designed, fabricated, and characterised for transfer/

TABLE I

POWER STANDARDS COMPARISON

Ref. Year	Freq (GHz)	Time (sec)	Resistance (Ω)	Matching Type	Remarks
This work	110-170	< 2.6	1600	Resonance	90% Response time; Bolometric Transfer Standard; Input power ~ 22.5 mW
[4] 2022	110-170	2400	205.5	Matched Load	Rise Time; Microcalorimeter; Input power ~ 31.5 mW
[17] 2021	140-220	~300	-	Matched Load	90% Response time (graph); Calorimetric; Reference Standard
[9] 2018	110-170	-	1000	Matched Load	Calorimeter element
[18] 2018	50-75	-	200	Resonance	Calorimeter; Thermistor mount
[19] 2018	75-110	-	-	Matched Load	Calorimeter using VDI Erickson PM5
[6] 2017	110-170	-	-	Matched Load	Calorimeter; Thermocouple
[20] 2016	75-110	0.2	-	Matched Load	90% Response time (20 mW scale); VDI Erickson PM5 with feedback
[21] 2015	75-110	-	50	Matched Load	Calorimetric Transfer Standard; Waveguide to CPW Transition
[8] 2015	110-170	-	-	Matched Load	Microcalorimeter
[10] 2010	75-110	~ 3000	-	Resonance	90% Time constant (graph); Thermistor Mount
[5] 2006	110-170	30	-	Matched Load	Response time (at 5 mW); Calorimeter with Feedback
[22] 2006	75-110	0.4	-	Matched Load	90% Response time (scale 20 mW); Calorimeter PM1B with feedback
[3] 1999	75-110	0.45	-	Matched Load	Time constant (scale 20 mW); Calorimeter with Feedback
[23] 1974	60-90	< 0.8	200	Matched Load	Response time of practical transducer; Thermocouple at resistive strip
[12] 1960	26.5-40	~ 15	609	Resonance	Time constant; Bolometer-Milliwatmeter
[24] 1958	8.20-12.40	15, 3	480-500	Resonance	Time constant of system (≥ 10 mW); 9.2 GHz; Thermocouple at the centre of film

working standard in the D-band. The power detector consists of two sensors A and B. The first is the main/active sensor to measure incident power, and the second is the dummy sensor for temperature compensation. As far as the author's knowledge, this is a unique type of barretter mount structure which has never been reported before in D-band or above. Other novelties and key features of the sensors are: (1) A resonance-type sensor covering the whole D-band. Resonant matching generally has poorer matching and narrowed bandwidth than matched load. We have used a folded-line structure to generate more matching points so as to increase the bandwidth to cover the whole D-band. (2) Fast response time. This is achieved through a compact design and effective thermal isolation. We have used quartz substrate and polyimide (Kapton) insulation tape. The sensor body is made of low thermal conductivity plastic (polyether ether ketone or PEEK). All help reduce the thermal time constant. (3) Temperature compensation using a compact dual-sensor configuration. This is to remove the impact of ambient temperature on the power measurement. These features and the portability of the sensor make it highly suitable as a transfer standard which is used to establish the traceability between the primary standard at the metrology organisation and industrial users.

In section II, the design and comparison between a single-line and a folded-line matching structure are explained. Section III shows the complete design of the power sensor. Section IV presents the fabrication and assembly. Section V discusses the power sensor characterisation before conclusions in Section VI.

II. THIN-FILM RESISTIVE LINE MATCHING STRUCTURE

The impedance matching and power sensing both rely on a thin-film resistive line. It uses a resonance-type matching technique which is inherently narrow band. We will first investigate and compare two matching structures with an objective to achieve a matched load across the D-band.

A. Single-Line Design

The conventional thin-film power detector only contains one section of the line placed at an off-set distance from the back-short. The circuit solution to such a line placed in a waveguide facing the input port has been detailed in [13]. Here a similar method is applied to a thin-film line facing the narrow wall of the waveguide instead, as shown in Fig. 1. This sidewall-facing E-plane configuration makes it convenient to accommodate more than one section of the line on the substrate in an effort to improve bandwidth, which will be discussed later in section B. The waveguide used is a standard D-band (WR-6) waveguide with internal dimensions of 1.651 mm by 0.826 mm.

The single resistive line is parallel to the electric field coming in the waveguide, and the electric field induces current oscillating in the line. The metallic thin-film line behaves as an inductor with a reactance X and a resistance R, as shown in the equivalent circuit in the inset of Fig. 2. The following can be written [13],

$$Z_{sc} = +j \cdot Z_0 tan(\beta l_s) \qquad (1)$$

$$Z_1 = \frac{Z_{sc} \times F_1}{Z_{sc} + F_1} \qquad (2)$$

where Z_{SC} is the short circuit impedance at a distance l_S from the back-short, which is in parallel to $F_1 = R + jX$, the impedance of the line. Z_1 is the overall equivalent input impedance.

The maximum current will only be induced and heat up the line when the structure in Fig. 1 is well matched. That is, the port should only see the purely resistive termination. The following two equations of matching conditions can be derived by equating the real term of (2) to Z_0 and the imaginary to zero [13],

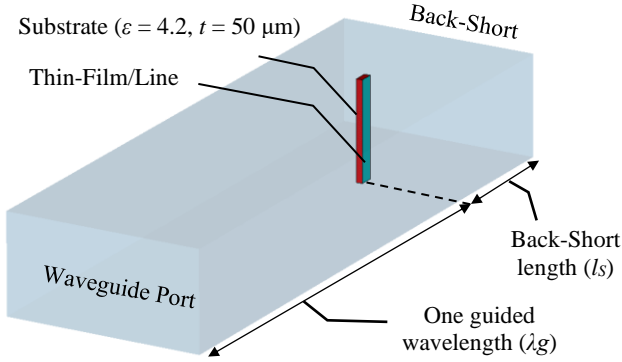$$X = \sqrt{R \cdot Z_0 - R^2} \qquad (3)$$

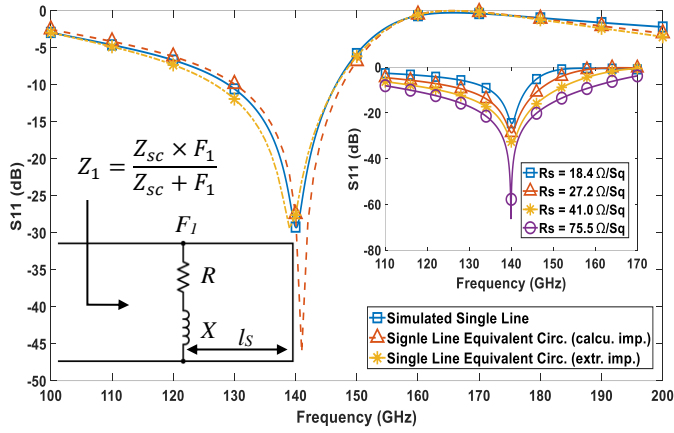**Fig. 1.** Single-line matching structure inside the waveguide shorted at one end.

Fig. 2. Simulated S_{11} of the matched single-line in Fig. 1 (with different sheet resistance, R_s), in comparison with the calculated responses from the circuit model. The inset shows the equivalent circuit diagram of the single-line design.

$$l_s = \frac{1}{\beta} \cdot \tan^{-1}\left(\frac{-R}{X}\right) \qquad (4)$$

where β is the propagation constant. The resistance, R, of the line depends on the material and its dimensions (length, width and thickness). The reactance, X, depends on the waveguide characteristic impedance, frequency and the width w of the line.

The impedance of the line can either be approximated using the analytical formula (for lines facing the port) given in [25] or extracted from the simulated reflection coefficient. To do so, the line is placed at the centre of a waveguide of a length of $2\lambda_g$ as shown in Fig. 3. The thin-film line impedance F can be linked to the linear reflection coefficient Γ as follows,

$$F = R + jX = -\frac{(1 + \Gamma)}{2 \cdot \Gamma} Z_0. \qquad (5)$$

Therefore, the equivalent R and X of the line can be extracted from the simulated reflection coefficient Γ.

Although the DC resistance of the power sensor element (thin-film line or thermistor) can usually be flexibly chosen,
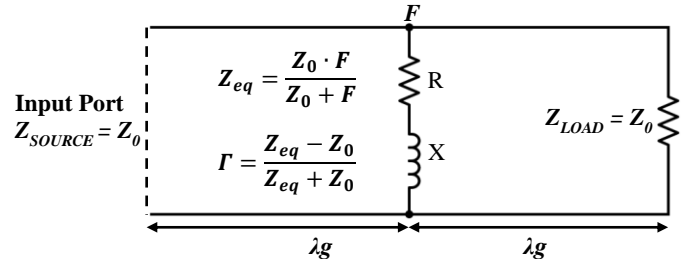

Fig. 3. Equivalent circuit diagram showing the method to extract the impedance of the thin-film line from the simulated reflection coefficient.

typically, this is around 200 Ω to match the widely available self-balancing bridge circuit in metrology [16], [26]. This value is initially chosen in this single-line design. It is worth noting that the R value is not prescribed for the final design.

Once R for the single-line design is chosen, the required X is determined from (3), and in turn, the back-short distance l_s can be found from (4). The length of the resistive line, in this case, equals to the internal height of the waveguide which is 0.826 mm. The width of the line w can either be found using the analytical formula in [17] or extracted from X using the method in Fig. 3. The sheet resistance R_S can be calculated by (6), which in turn can be used to determine the required film thickness t,

$$R_s = \frac{1}{\sigma \cdot t} = \frac{R \cdot w}{l}. \qquad (6)$$

As an example, at the central frequency (140 GHz) of the D-band, the line width is found be 112 μm from the simulation. The extracted impedance of the line is 231+j233 Ω. The back-short distance l_s is calculated to be 1.059 mm from (4). The required sheet resistive is 27.2 Ω/Sq.

From Fig. 2, it can be seen that the calculated response from the equivalent circuits agrees well with the full-wave simulation using CST Studio Suite, which validated the circuit approach. Further simulation from Fig. 2 shows that a higher sheet resistance R_S (corresponding to a higher R value) would improve the impedance matching. However, it also means thinner film is required. For instance, if the widely used platinum is to realise the sheet resistance of 27.2 Ω/Sq, the film thickness would be 4 nm based on its nominal conductivity of 9.434 ×10^6 S/m. This thickness would cause difficulty in term of its reproducibility in deposition. Fig. 2 also indicates, as expected, that the single-line solution only offers limited bandwidth.

B. Folded-Line Design

To enhance the matching bandwidth, a folded-line structure is proposed as shown in Fig. 4. The design has used the knowledge gained from equivalent circuit analysis. At the start of the design process, only the two vertical sections of the folded-line are considered to simplify the circuit analysis. The idea is to create more matching points across the band, so the

TABLE II
DESIGN PARAMETERS FOR 200 Ω RESISTANCE AT THREE
DIFFERENT FREQUENCIES

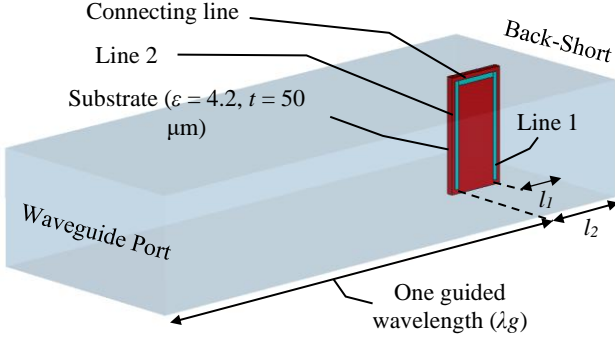| Design frequency (GHz)	120	140	160
Chosen DC line (Single) resistance (Ω)	200	200	200
Line width (μm)	64	112	157
Sheet resistance (Ω/Sq)	15.6	27.2	38

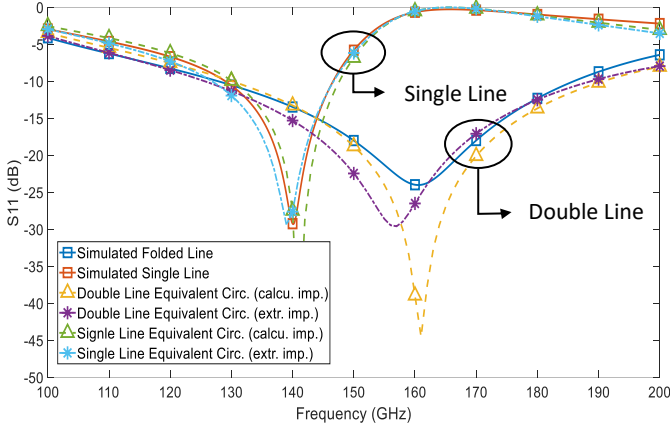**Fig. 4.** Folded-line matching structure inside the waveguide shorted at one end.

Fig. 5. Comparison of reflection coefficient curves obtained from the simulation and the equivalent circuit
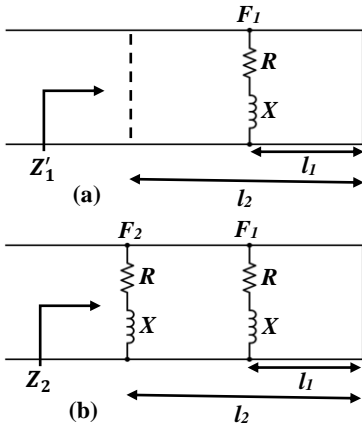

Fig. 6. Equivalent circuit diagram of the two lines: (a) Before adding Line 2, (b) After adding Line 2.
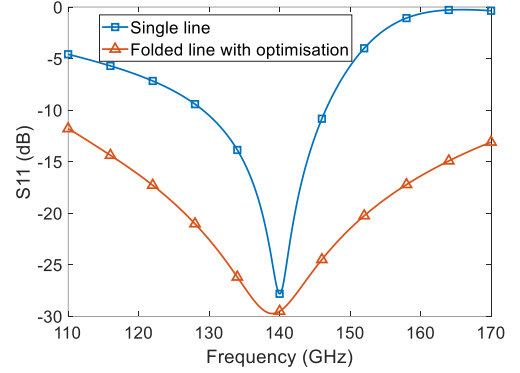

Fig. 7. Simulated S_{11} of the optimised single and folded-line structures ($R_S = 27.2$ Ω/Sq).

initial dimensions of the matched single-line at three different frequencies (120, 140, and 160 GHz) are first obtained from (3) – (5). These parameters are given in Table II. The impedances of these three lines are extracted from the simulated reflection coefficient as in Fig. 3. The corresponding back-short lengths can then be calculated from (4). For the initial design, as a comprise, the sheet resistance is chosen to be the value obtained from the central frequency of 140 GHz, i.e., 27.2 Ω/Sq, whereas the off-sets of the two lines (Line 1 and Line 2 in Fig. 4) are chosen to be the values obtained for 120 and 160 GHz, respectively. It is observed that using small line width improves return loss. After optimisation, the response in Fig. 5 is obtained where $w =$ 0.032 mm, $l_1 = 0.903$ mm and $l_2 = 0.533$ mm. Note that still only the two vertical sections of the line are considered so far.

Figure 6 shows the equivalent circuit diagram of the dual-line structure, excluding the connecting strip that joins the two lines. Assume the impedance of both lines is the same ($F_1 = F_2$). The input impedance seen at a distance of l_2 to the back-short, excluding the parallel Line 2 is,

$$Z_1' = Z_0 \frac{Z_1 + jZ_0 tan\beta(l_2 - l_1)}{Z_0 + jZ_1 tan\beta(l_2 - l_1)} \qquad (7)$$

where Z_1 is the input impedance seen at a distance of l_1 to the back-short and given in (2). Therefore, the overall input impedance, Z_2, is a result of parallel Z_1' and the line impedance of F_2, i.e.,

$$Z_2 = \frac{Z_1' \times F_2}{Z_1' + F_2} \qquad (8)$$

The calculated impedance based on the line dimension as well as the extracted impedance from CST, are used in (8). The calculated S-parameter responses from these two different approaches agree very well, as shown in Fig. 5. They are also in good agreement with the simulated responses. It is important to note from Fig. 6 that the two-line design has much wide bandwidth than the single-line design. However, the matching point of the two-line design is shifted upward to about 160 GHz. At this point, a horizontal line is added to

connect the two vertical lines, forming a dc path as required for sensor readout. This lowers the matching frequency and worsens the matching. After further optimisation ($w = 0.035$ mm, $l_1 = 0.773$ mm and $l_2 = 0.403$ mm), the matching point is corrected back to 140 GHz. As shown in Fig. 7, a return loss of over 10 dB can be achieved across the D-band. The advantage of the bandwidth is again very clear from the comparison with an optimised single-line design based on the same sheet resistance of 27.2 Ω/Sq. It should be noted that the DC resistance (R) of the folded-line has been increased to 1.96 kΩ.

III. COMPLETE DESIGN

The actual sensor with the presented folded-line structure will be housed in D-band waveguide with a UG-387 flange. The sensor chip will be fitted into a holding recess and inserted into the waveguide along the E-plane, as shown in Fig. 8. The complete design consists of the main sensor (sensor A) for detecting incident microwave power and the dummy sensor without a flange (sensor B) for detecting ambient temperature variation. The sensor housing needs to be designed to allow for secure installation of the sensor chip and to thermally isolate it from ambient temperature drift

The sensor chip is 6.6 mm × 2.0 mm × 0.1 mm (length × width × thickness) in size, as illustrated in Fig. 9. Substrate materials with low thermal conductivity such as polyimide (thermal conductivity = 0.12 W/m·K) and quartz (3 W/m·K) are good options. A quartz substrate ($\varepsilon = 3.75$, thickness of 100 μm) is chosen to fabricate the sensor chip. The polyimide tape is used to hold the chip securely in the rectangular slot and to isolate the chip from the housing.

The material for the sensor line should have high temperature coefficient, high resistivity and be compatible with the quartz substrate in fabrication. Nichrome [12][13], nickel [14][15], and platinum [24] materials have been mostly used as sensing elements. Titanium has also been used for detecting terahertz [27] and infrared [28] radiations. Titanium has higher resistivity (430 nΩ·m) than Platinum (106 nΩ·m), while both have similar temperature coefficients. Therefore, titanium is chosen for the thin-film line, for ease of fabrication, which allows a larger film thickness (15.5 nm) than a platinum line (4 nm) to achieve the same sheet resistance of 27.2 Ω/Sq. Two gold-coated pads are added for DC connection above the line, as shown in Fig. 9. Two spring-loaded DC connection pins press down from the holes for each sensor, as shown in Fig. 8.

Several changes have been made to fit the folded-line design (Fig. 4) in the housing. The substrate size has to be increased to accommodate the DC pads. This has led to leakage through the substrate and spurious resonances. The reflecting-strip was added to limit the signal leakage to the large side cavity containing the substrate and reduce the spurious resonances at higher frequencies. It has also helped to align the polyimide tape after fabrication. Polyimide wrapping is used to isolate the chip from the surrounding body and to fit into the housing. This has also affected the matching but not in a significant way, as shown in Fig. 10 when different thicknesses of the wrapping (0, 250, and 500 μm) around the chip
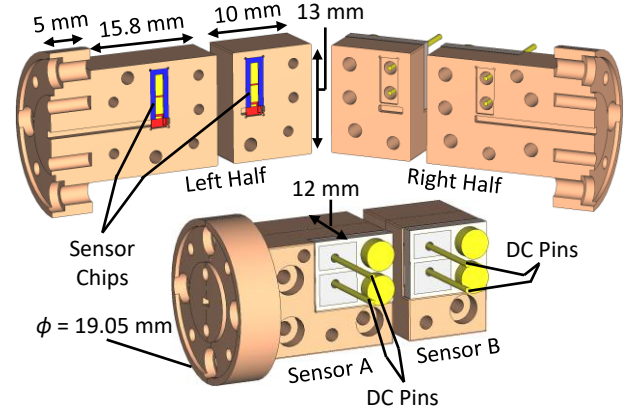
Fig. 8. Illustration of the detector housing, showing the chip placement.
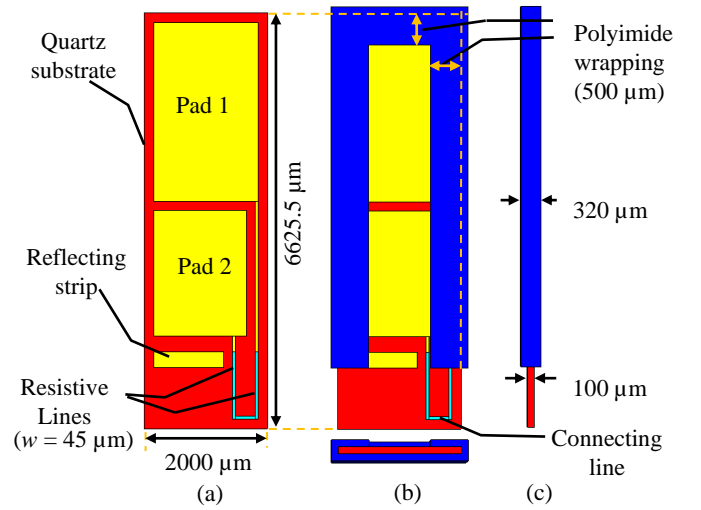
Fig. 9. Layout of the sensor chip: (a) chip (b) chip covered in polyimide (c) side view.
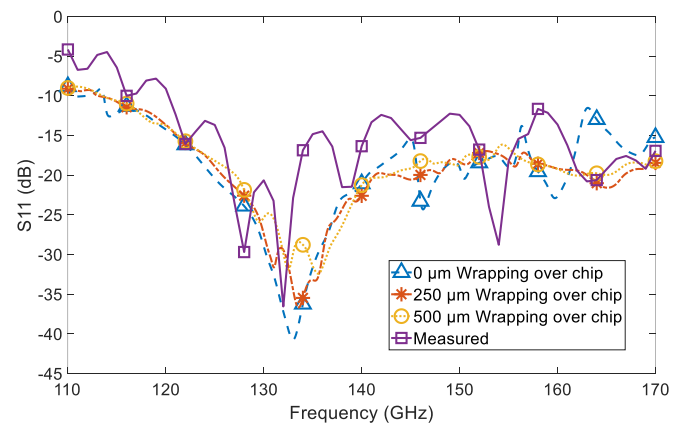
Fig. 10. Simulated result of the final design model with the housing compared to the measurement.

are simulated to see the effect on S_{11}. Also shown in Fig. 10 is the matching point in the simulated S_{11} that has shifted from 140 to 132 GHz. Some ripples appear, which is believed to be a result of some weak resonances from the recess used to hold

Fig. 11. Design of sensor A and B in thermal shielding.

Fig. 13. Fabricated sensors A and B in thermal shielding.

the chip and the gaps around the chip in the waveguide. The measured reflection coefficient from Section V is also plotted with the simulated S_{11} in Fig. 10 for com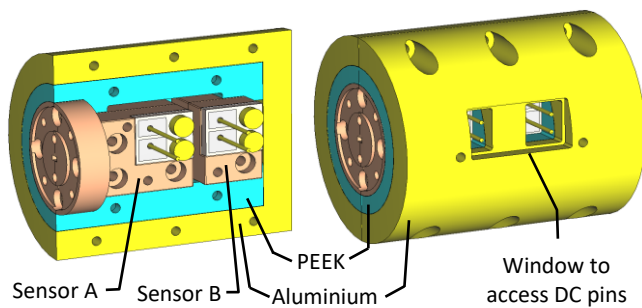parison, they are in good agreement. The final updated parameters are w = 0.045 mm, l_1 = 0.803 mm and l_2 = 0.433 mm. The DC resistance of the sensor is calculated to be 1.5 kΩ.

The two sensors (A and B) should be placed together to ensure the sensing of the same ambient temperature and simultaneously be thermally isolated from each other. The latter is facilitated by an air gap of 2 mm. The sensor B is used to compensate out the ambient temperature variations from sensor A so that the absolute RF power can be measured. The sensors are also found to be very sensitive to handling and airflow, so they are shielded, as shown in Fig. 11. The inner shielding is made of PEEK material, and the outer one is made of aluminium.

IV. SENSOR FABRICATION

The fabricated sensor chips are shown in Fig. 12(a). The titanium thin film was evaporated on the quartz substrate. At the nominal thickness of 15.5 nm, the measured sheet resistance is 79.3 Ω/sq, about three times higher than the design requirement. The film thickness is therefore increased to reach 27 Ω/sq. The DC pads were coated with gold of 100 nm. The measured resistance of the folded-line is ~1.6 kΩ
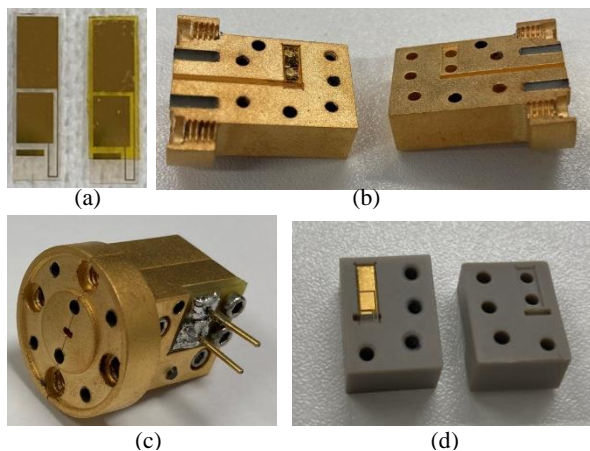

Fig. 12. Fabricated sensors: (a) Sensor chips before and after wrapping with polyimide; (b) Sensor A in split blocks; (c) Assembled Sensor A; (d) Sensor B in split blocks with the chip installed.
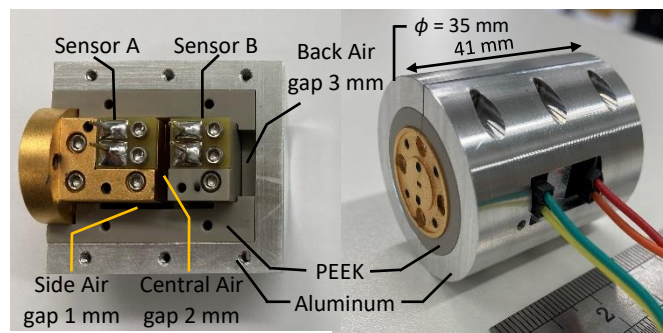
which is consistent with the design. 50 µm thick polyimide tape was used to wrap the chip and fit it into the housing.

As shown in Fig. 12 (b) - (d), the sensor bodies are made out of the thermoplastic polymer PEEK, which has a low thermal conductivity of 0.25 W/m·K, to reduce the effect of surrounding temperature drift. The body of Sensor A is gold-plated, whereas Sensor B is not plated, as it does not carry any microwave signal. The absence of the gold coating also helps with thermal isolation.

Sensors A and B are placed inside the shielding (shown in Fig. 13), which helps with the handling and reduces the effect of ambient temperature fluctuation. The shielding also ensures a similar ambient environment for both sensors. The sensor bodies are held inside the PEEK shielding only at the corners. There is an air gap of 1 mm surrounding it for thermal isolation. The air gap between the sensors is kept 2 mm. This will minimise the amount of heat exchange between the sensor A and B. All these measures aim to reduce the correlation between the two sensors so that Sensor B can trace the ambient temperature only. The size of the cylindrical aluminium shielding is 35 mm × 41 mm (outer diameter × length), which is comparable to that of the commercially available PM5 (51 mm × 48 mm × 76 mm).

V. SENSOR CHARACTERIZATION

The performance of the sensor has been evaluated through the measurement of voltage reflection coefficient (VRC or S_{11}), short- and long-term time responses, linearity and frequency response as described in [4]. These parameters can be used to characterize the sensor behaviour when a microwave signal is incident for real applications.

A. Voltage Reflection Coefficient, VRC or S_{11}

The VRC of sensor A was measured using a vector network analyser (VNA) with a D-band waveguide extender. A D-band calibration kit was used to calculate the error terms of the VNA-extender combination using a through-reflect-line calibration methodology. Sensor A was connected to the extender's waveguide port. VRC was measured and is illustrated in magnitude and phase in Fig. 14. The sensor output was not connected to any other instrumentation during this measurement.

The measured VRC shows good agreement with the simulation, as shown in Fig. 10. The VRC magnitude of the

Fig. 14. VRC measurements of sensor A.

Fig. 15. Measurement setup for time response characterization of the sensor.
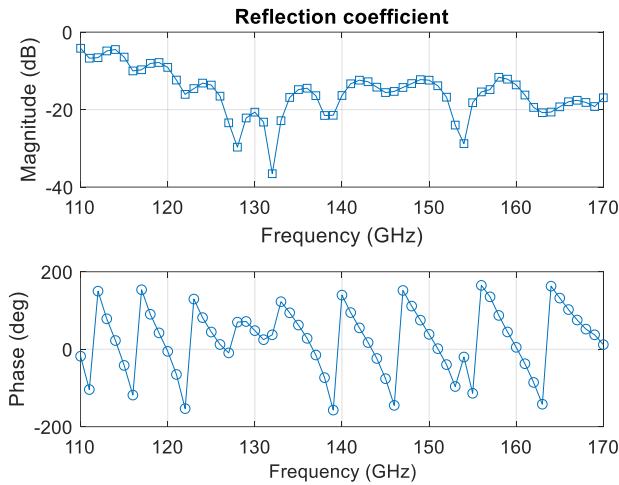
sensor is - 4.2 dB at 110 GHz and decreases as the frequency increases. It is lower than -11.5 dB for frequencies greater than 120 GHz. The phase of the sensor in Fig. 14 shows good continuity except for around 130 and 155 GHz, where the VRC magnitude is small. This is due to the uncertainty in the phase being related to the magnitude of the VRC and its associated uncertainty. When the magnitude is close to 0 (infinite in dB scale) and less than its uncertainty, the phase becomes undefined and can therefore be described as fully uncertain.

B. Short-Term Time Response

To characterize the short-term time response, the setup shown in Fig. 15 was used. A signal generator, including a WG29 multiplier was used to produce the necessary microwave signal and an attenuator was used to adjust the power level. This power flows through a 10 dB directional coupler whilst a small portion is coupled to port 3 where it can be measured by a commercial power sensor/meter combination (VDI Erickson PM5) [20], with its indication acting as a reference power. The shielded sensor A and B combination (Fig. 13) was connected to port 2 of the directional coupler, where a fixed proportion of the input power was incident upon. An Ohm-meter was connected to each of the sensor outputs A and B, respectively to measure the sensor's resistance.

To ensure that thermal equilibrium of the system had been reached, the sensor and system setup were connected and allowed to settle for 24 hours prior to measurement. Measurements were performed for power off and on, respectively, at 140 GHz. This frequency was chosen because of the relatively small VRC magnitude of the Sensor A. The measurement sequence began with a reading of the resistance of Sensor A and B using the ohm-meters with the power off for ~175 minutes. Power was then applied to sensor A while the output from ohm-meters were monitored. During all these measurements the output of the PM5 was also monitored. The time interval between two measurements from the same sensor was ~2.6 s and named as the measurement system response
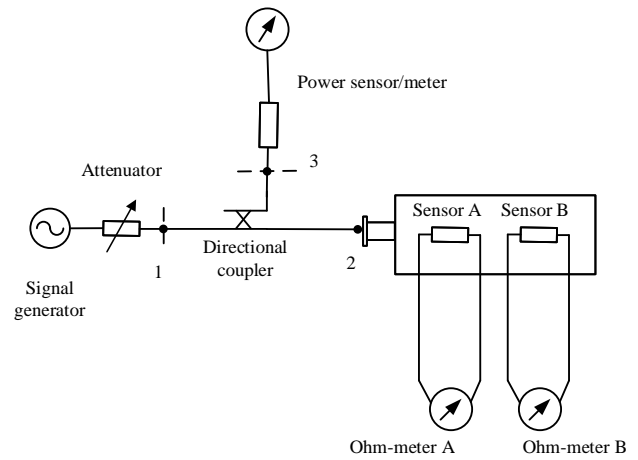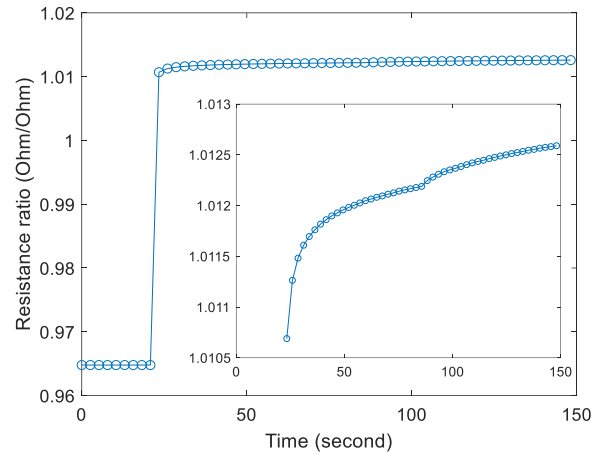

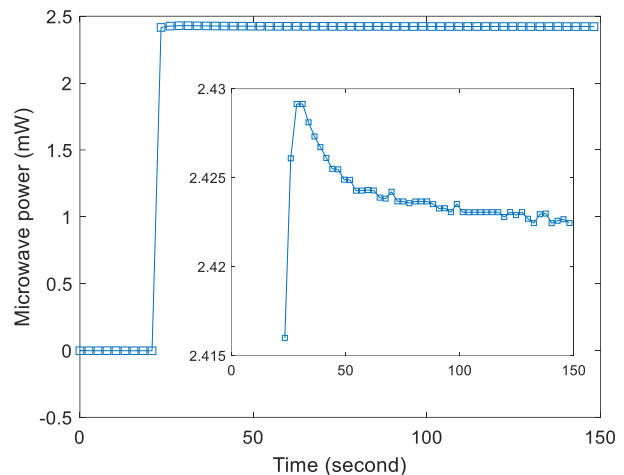**Fig. 16.** Short-time response of the mounted sensor at 140 GHz.

Fig. 17. The commercial PM5 sensor/meter combination power response under the same condition as the mounted sensor.

time. It should be noted that this time is limited by the response of our ohm meters, computer and cable delays. The estimated response time of the sensor itself (without any

feedback) should be less than 2.6 s. This is competitive with commercial PM5 sensors. The time constant of the basic sensor in PM5/PM5B is 6 s [20]. Feedback electronics have been used to get a fast response time, whereas our sensor is raw.

The resistance ratio between sensor A and B was used to show the short-term response of the mounted sensor combination. This ratio eliminates the dependency of the sensor resistance on the ambient temperature and its variation effect on sensor A. The ratio of these resistances for the off and on states is shown in Fig 16. The sensor response time is much shorter (< 2.6 s) than the measurement system. The resistance of sensor A and B, measured with the system at thermal equilibrium and without any incident power was 1578.5 Ω and 1633.8 Ω respectively, giving a resistance ratio of 0.9662. After power was incident onto the sensor, the resistance ratio deviated slightly from the ratio of 1.0107 at approximately 25s to that of 1.0126 after 125s. This is a variation of 0.19% over this period. Given a typical measurement period of nominally 2 min for general applications, a test interval of 125 s was selected to calculate the mounted sensor deviations. The deviation of the reference power from the PM5 was also calculated for the same period and is depicted in Fig. 17. The deviation for the PM5 sensor was 0.27% for a nominal 2.5 mW power. The two deviations are very close to each other and shows that the mounted sensor has very good short-time response.

C. Long-Term Time Response

The other time dependent parameter to assess for the mounted sensor is the long-term response and how the sensor repeats with the power switched multiple times. The same setup as the short-term response measurement was used here. The measurement sequence was powered off-on-off-on-off, with each off and on lasting 175 minutes. The outputs of sensor A, sensor B and the reference power were measured at the same system time response interval as previously. The resistance ratio was once again recorded to eliminate the ambient temperature effect on the mounted sensor. This ratio and the measured reference power for each sequence are shown in Fig. 18. To evaluate the mounted sensor performance, the measured reference power by the PM5 sensor was used. The average and experimental standard deviation for each individual sequence (total of 4050 measurement points) were calculated and given in Table III. The standard deviations of the resistance ratios are consistent whereas those for the reference powers are different. This is due to the zeroing process of the commercial sensor. To make the two parameters more comparable, the difference between the ON and OFF parameters given in Table III was used. This difference in the reference power was 2.39931 mW and 2.38535 mW for the first and second power on-off cycles, respectively. For the mounted sensor, the resistance ratios were 0.04709 Ω/Ω and 0.04734 Ω/Ω.

The ratio of the standard deviations relative to the calculated differences is a more meaningful indicator of the
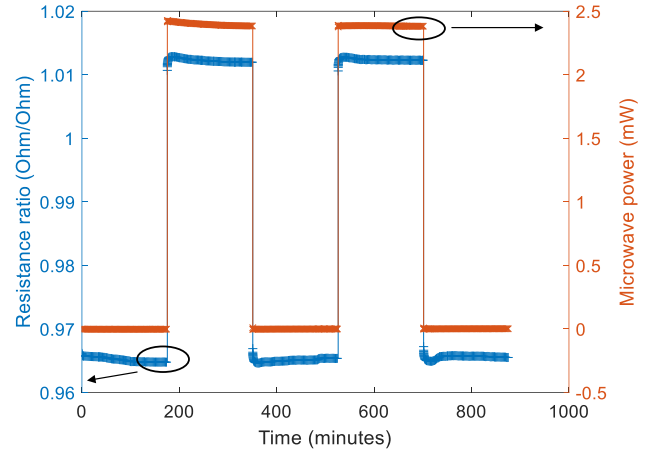

Fig. 18. The resistance ratio and reference power for the power off and on sequences at 140 GHz.

TABLE III
AVERAGE AND EXPERIMENTAL STANDARD DEVIATION FOR EACH SEQUENCE.

Sequence	Average		Standard deviation	
	Microwave power (mW)	Ratio (Ω/Ω)	Microwave power (mW)	Ratio (Ω/Ω)
Power off-1	-0.00198	0.96516	0.00028	0.00035
Power on-1	2.39733	1.01226	0.01162	0.00028
Power off-2	-0.00080	0.96506	0.00049	0.00023
Power on-2	2.38455	1.01240	0.00149	0.00016
Power off-3	0.00101	0.96559	0.00043	0.00024

sensor performance, allowing for direct comparison. The standard deviation ratios for the reference power were obtained as 0.484% and 0.062% for the first and second power on-off sequences, whilst for the mounted sensor these were 0.594% and 0.338%. This shows that the deviation of the mounted sensor is less than 0.6% and similar to the commercial power sensor.

D. Frequency Response

The frequency response (F_R) is a transfer function defined as the change of the mounted sensor's output resistance with respect to the incident microwave power onto the mounted sensor. This was calculated using (9), derived for the measurement setup in Fig. 15 using a 3-port power splitter methodology. The measurement was performed from 110 GHz to 170 GHz at a step of 5 GHz. A characterized PM5 sensor/meter [29] was used to monitor the microwave power at Port 3.

$$F_R = EE \frac{\Delta R}{P_{STD}} \frac{|S_{31}|^2}{|S_{21}|^2} \frac{1 - |\Gamma_{STD}|^2}{1 - |\Gamma_{MS}|^2} \frac{|1 - \Gamma_2 \Gamma_{MS}|^2}{|1 - \Gamma_3 \Gamma_{STD}|^2} \quad (9)$$

where EE is the effective efficiency of the PM5 sensor/meter given in [29], P_{STD} is the measured microwave power from the power sensor/meter, S_{31} and S_{21} are voltage transfer
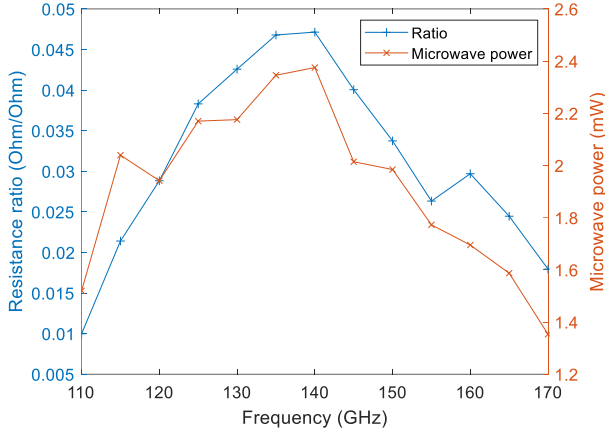
Fig. 19. Measured power from the sensor/meter and the resistances ratio of sensor A and B for a 3-min waiting time interval.
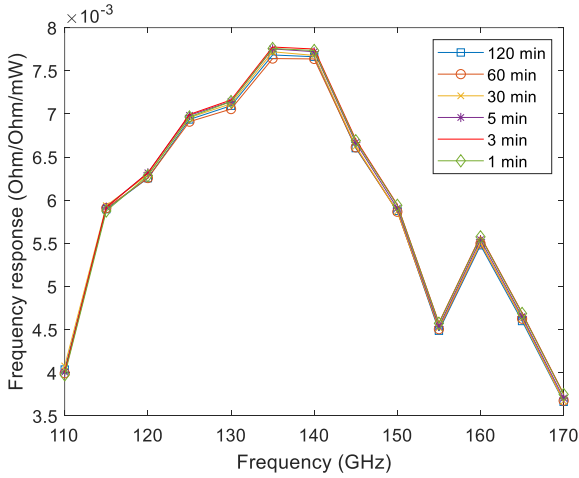

Fig. 20. The frequency response for different waiting time intervals.
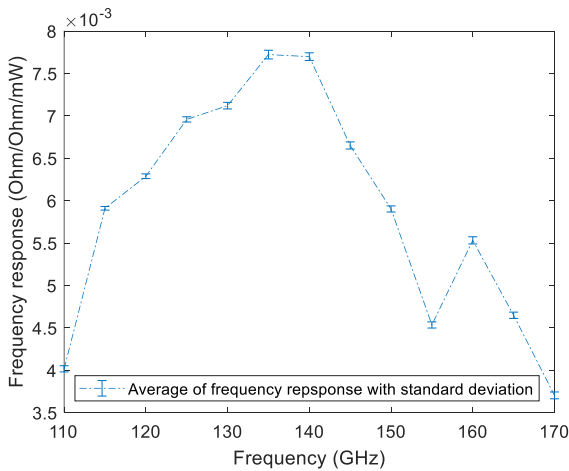

Fig. 21. Average and standard deviation of the frequency response.

coefficients from port 1 to 3 and from port 1 to 2, respectively. Γ_{MS} is the voltage reflection coefficient of the mounted sensor, Γ_{STD} is that of the power sensor/meter, Γ_2 and Γ_3 are those of

port 2 and 3 of the directional coupler, and ΔR is the difference between the resistance ratios for microwave off and on for sensor A and sensor B.

The measurement was performed, firstly, for microwave power off, measuring sensor A and sensor B resistances and the power meter/sensor output power with 150 samples taken and average. Afterwards, microwave power was applied to the directional coupler incrementally from 110 GHz to 170 GHz, and the aforementioned parameters were measured again at each frequency. The ratio for the resistance changes of sensor A and B were calculated for all measured points including power off. The difference between the ratios with respect to each frequency point and power off was used as the ΔR parameter.

The frequency response for different waiting time intervals between the two measurement points (e.g., two consecutive frequency points) was analysed with waiting times between 1 and 120 minutes. The measured ΔR and P_{STD} for a waiting interval of 3 minutes are illustrated in Fig. 19.

The frequency responses for different waiting times (1, 3, 5, 30, 60 and 120 minutes) were calculated using (9) and shown in Fig. 20. An average of all measurements with standard deviation is shown in Fig. 21. The minimum and maximum standard deviation at one-sigma were 0.36% (115 GHz) and 0.66% (135 GHz). This shows that the mounted sensor has very reproducible frequency response between 1 – 120 min intervals.

E. Linearity

Linearity is a parameter that shows how the mounted sensor's response behaves at different input power levels at a single frequency. The measurement setup in Fig. 15 was used. The input power was varied from -10 dBm to 9 dBm for each frequency from 110 GHz to 170 GHz at 5 GHz steps using the waveguide attenuator. The resistances of Sensor A and B and the reference power were monitored. The microwave power was worked out using the resistance ratios for each measured point and the frequency response (Fig 21) of the mounted sensor. The mounted sensor response at +5 dBm at each frequency was used as a reference. The measured deviation from this reference was plotted in Fig. 22. It can be observed the deviation varies between ±1.5 dB and ±0.6 dB from -10 dBm to -3 dBm. Above this power level, the deviation is within ±0.25 dB. The deviation at 110 GHz is the highest due to the relatively high VRC.

VI. CONCLUSION

A D-band thin-film bolometer with a unique folded-line structure in the E-plane was designed, fabricated and characterized as a transfer standard. The circuit analysis and simulations show the folded-line structure improves bandwidth. The effect of ambient temperature drift is reduced in this design by using low thermal conductive materials for the sensor chip (quartz), its wrapping (polyimide) and the detector housing (PEEK). The compensation sensor (B) detects the ambient variation and removes its impact on the
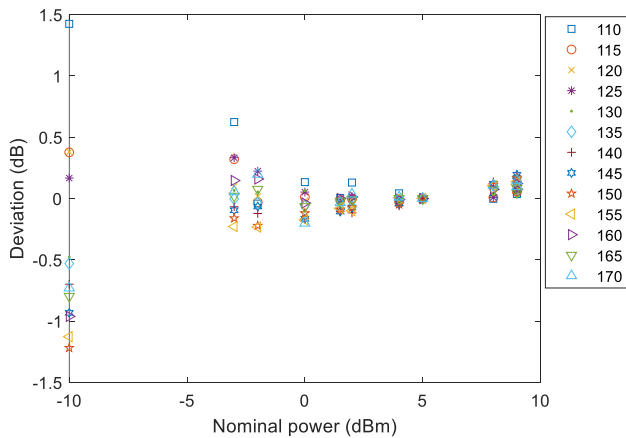
Fig. 22. The Linearity of the mounted sensor from 110 GHz to 170 GHz in 5 GHz step.

power sensor. The device is successfully characterized as a transfer/working standard which can be used in ambient temperature environments. The measured return loss is above 10 dB from 122 GHz to 170 GHz. The deviation in the sensor's response (0.19 %) for the given short-time interval is very close to the commercial sensor (0.27 %). The sensor exhibits very good short-time response with a response time much better (< 2.6 s) than the measurement system. The long-term time response showed that the sensor is thermally very well isolated from the surrounding, and the standard deviation is less than 0.6 %. This indicates the sensor performs excellently. However, the lowest power that can be measured depends on the acceptable deviation from linearity. From -3 dBm to 10 dBm, the deviation is limited within ±0.6 dB.

REFERENCES

[1] P. H. Siegel, "Terahertz Technology," *IEEE Trans. Microw. Theory Tech.*, vol. 50, no. 3, pp. 910–928, 2002.
[2] X. Shang, M. Ke, Y. Wang, and M. J. Lancaster, "WR-3 band waveguides and filters fabricated using SU8 photoresist micromachining technology," *IEEE Trans. Terahertz Sci. Technol.*, vol. 2, no. 6, pp. 629–637, 2012.
[3] N. Erickson, "A Fast and Sensitive Submillimeter Waveguide Power Meter," *Tenth International Symposium on Space Terahertz Technology.* pp. 501–507, 1999.
[4] M. Salek *et al.*, "Design, Fabrication, and Characterization of a D-Band Bolometric Power Sensor," *IEEE Trans. Instrum. Meas.*, vol. 71, pp. 6–14, 2022.
[5] J. A. Mallat, S. N. Dudorov, D. V. Lioubtchenko, and A. V. Räisänen, "110-170 GHz millimetre wave power standard," *Proc. 36th Eur. Microw. Conf. EuMC 2006*, no. September, pp. 482–485, 2006.
[6] W. He, W. Zhang, W. Qi, and H. Yin, "Design of a 110GHz to 170GHz calorimeter," *2017 Int. Work. Electromagn. Appl. Student Innov. Compet. iWEM 2017*, no. 1, pp. 71–73, 2017.
[7] Y. Tojima, M. Kinoshita, H. Iida, and K. Fujii, "Development of WR-5 Waveguide Calorimeter for Millimeter Wave Power Standard," *CPEM 2018 - Conf. Precis. Electromagn. Meas.*, pp. 1–2, 2018.
[8] C. Ma, X. Cui, W. Yuan, and Y. Li, "Design of a WR-6 thermoelectric conversion power sensor," *IRMMW-THz 2015 - 40th Int. Conf. Infrared, Millimeter, Terahertz Waves*, vol. 6, pp. 1–2, 2015.
[9] X. Wang, Q. Zhong, J. Li, W. Yuan, Y. Li, and X. Cui, "WR-06 Power Standard Devices," *CPEM 2018 - Conf. Precis. Electromagn. Meas.*, pp. 1–2, 2018.

[10] D. Adamson, J. Miall, J. Howes, M. Harper, and R. Thompson, "A new 75-110 GHz primary power standard with reduced thermal mass," *75th ARFTG Microw. Meas. Conf. Meas. Modul. Signals Commun.*, pp. 1–4, 2010.
[11] J. Y. Kwon, Y. P. Hong, D. J. Lee, and T. W. Kang, "V- and W-band waveguide microcalorimeters for millimeter-wave power standards," *85th ARFTG Microw. Meas. Conf. Meas. Tech. 5G Appl. ARFTG 2015*, pp. 1–3, 2015.
[12] I. Lemco and B. Rogal, "Resistive-Film Milliwattmeters For The Frequency Bands 8.2-12.4Gc/s, 12.4-18Gc/s and 26.5-40Gc/s," *Inst. Electr. Eng. Sep. 1960*, vol. 16, no. 3298, pp. 16–19, 1960.
[13] J. A. Lane and D. M. Evans, "The design and performance of transverse-film bolometers in rectangular waveguides," *Proc. IEE Part B Electron. Commun. Eng.*, vol. 108, no. 37, p. 133, 1961.
[14] K. Sukurai and T. Nemoto, "A Thin-Film Bolometer Unit," *IEEE Trans. Instrum. Meas. Sept. 1967*, vol. IM, no. 3, pp. 206–211, 1967.
[15] T. Inoue, I. Yokoshima, and M. Sasaki, "High-Performance Thin-Film Barretter Mount For Power Measurement In W-Band," *Electron. Lett.*, vol. 21, no. 5, pp. 170–172, 1985.
[16] L. Brunetti, "Thin-film bolometer for high-frequency metrology," *Sensors Actuators A. Phys.*, vol. 32, no. 1–3, pp. 423–427, 1992.
[17] Y. Tojima, M. Kinoshita, H. Iida, and K. Fujii, "Calibrating Power Meters in the 140-220-GHz Frequency Range Using an Absolute-Power Reference Calorimeter," *IEEE Trans. Instrum. Meas.*, vol. 70, 2021.
[18] D. Gu, X. Lu, B. F. Jamroz, D. F. Williams, X. Cui, and A. W. Sanders, "NIST-Traceable Microwave Power Measurement in a Waveguide Calorimeter with Correlated Uncertainties," *IEEE Trans. Instrum. Meas.*, vol. 68, no. 6, pp. 2280–2287, 2019.
[19] J. Y. Kwon, Y. P. Hong, and N. W. Kang, "D-Band Waveguide Microcalorimeter for Millimeter-Wave Power Standard," *CPEM 2018 - Conf. Precis. Electromagn. Meas.*, pp. 1–2, 2018.
[20] Virginia Diodes Inc, "PM5 Operational Manual," vol. 6172, Charlottesville, VA, USA, p. 22, 2016.
[21] R. H. Judaschke, K. Kuhlmann, T. M. Reichel, and W. Perndl, "Millimeter-Wave Thermoelectric Power Transfer Standard," *IEEE Trans. Instrum. Meas.*, vol. 64, no. 12, pp. 3444–3450, 2015.
[22] Y. S. Lau, T. Denning, and C. Oleson, "Millimeter wave power measurement above 110 GHz," *2006 67th ARFTG Microw. Meas. Conf. - Meas. Des. High Power Devices Syst.*, pp. 97–102, 2006.
[23] H. Toda, K. Sasaki, Y. Nakagawa, and I. Sugiura, "Matched-Load-Type Thermoelectric Transducer for Power Measurements in the Millimeter Wave Region.," *IEE Conf. Publ.*, vol. IM, no. 113, pp. 188–190, 1974.
[24] J. A. Lane, "Transverse film bolometers for the measurement of power in rectangular waveguides," *Proc. IEE - Part B Radio Electron. Eng.*, vol. 105, no. 19, pp. 77–80, 1958.
[25] N. Marcuvitz, *Waveguide Handbook*, First. McGraw-Hill Book Company, Inc, 1951.
[26] X. Cui, Y. S. Meng, Y. Shan, and Y. Li, "Microwave Power Measurements: Standards and Transfer Techniques," *New Trends Dev. Metrol.*, pp. 3–20, 2016.
[27] N. Hiromoto *et al.*, "High Responsivity and Low NEP of Room-Temperature Terahertz Antenna-Coupled Microbolometers with Meander Titanium Thermistor," *Int. Conf. Infrared, Millimeter, Terahertz Waves, IRMMW-THz*, vol. 2019-Septe, 2019.
[28] R. S. Saxena, R. K. Bhan, C. R. Jalwania, and K. Khurana, "Effect of excessive bias heating on a titanium microbolometer infrared detector," *IEEE Sens. J.*, vol. 8, no. 11, pp. 1801–1804, 2008.
[29] M. Celep, M. Salek, D. Stokes, J. Skinner, and Y. Wang, "Power Sensor Characterization from 110 to 170 GHz Using a Waveguide Calorimeter," *IEEE Trans. Instrum. Meas.*, vol. 71, 2022.